Main results of the analysis of the HOMER Lagrangian Particle Tracking and Data Assimilation database

Andrea Sciacchitano[1,*], Benjamin Leclaire[2], Andreas Schröder[3]
1: Faculty of Aerospace Engineering, Delft University of Technology, Delft, the Netherlands
2: Department of Aerodynamics, Aeroelasticity and Acoustics, ONERA, Meudon, France
3: Institute of Aerodynamics and Flow Technology, DLR, Göttingen, Germany
* Correspondent author: a.sciacchitano@tudelft.nl

Keywords: Lagrangian Particle Tracking, Data Assimilation, moving panel, benchmark database

ABSTRACT

In this work, we extend the analysis of Lagrangian Particle Tracking (LPT) and Data Assimilation (DA) algorithms, presented at the ISPIV21 conference, to the case of a turbulent wall-bounded flow interacting with a moving panel. The work is conducted within the European project HOMER and the data is processed by the partners of the project consortium. A synthetic experiment is performed that reproduces the air flow around a cylinder in ground effect, whereby a flexible panel is placed undergoing periodic oscillations. The database comprises two different panel's materials, namely metal and rubber, different marker densities on the panel's surface and different concentrations of tracer particles in the flow. Images of the flow tracers and of the surface markers are acquired either with a four-camera volumetric imaging setup or with a dual setup composed of four LPT cameras and two Digital Image Correlation (DIC) cameras. Additionally, three image acquisition modes are simulated, namely time-resolved, two-pulse and four-pulse. The data are analyzed in terms of percentages of correctly reconstructed, missed and ghost particles, errors of the measured particles' positions, velocities and accelerations (LPT analysis) and errors of the reconstructed flow fields, panel's positions and surface pressures (DA analysis).

1. Introduction

In the last three decades, Particle Image Velocimetry (PIV) has evolved into the chief technique for fluid flow measurements. While the introduction of tomographic PIV (Elsinga et al., 2006) first enabled three-component flow velocity measurements in three-dimensional domains, the advent of time-efficient Lagrangian Particle Tracking (LPT) algorithms greatly reduced the computational time while allowing for more accurate reconstructions of the three-dimensional particles distributions at relatively high seeding densities (Kähler et al., 2016; van Gent et al., 2017). One of the most commonly used LPT algorithms is the Shake-The-Box (STB) approach introduced by the DLR group (Schanz et al., 2016), together with its evolutions for multi-pulse multi-exposure measurements (Novara et al., 2016, 2019). The STB algorithm relies on the Iterative Particle Reconstruction (IPR, Wieneke, 2012, Jahn et al., 2021) and makes use of the temporal information to predict and correct the particles' positions at successive time instants.

Alternative approaches to STB have been proposed where the particles' correction phase ("shaking") is conducted via the ensemble technique, as discussed in Yang et al. (2018), or via Kernel methods as in the Kernelized Lagrangian Particle Tracking technique (KLPT, Yang and Heitz, 2021). To enhance the initialization of new tracks, an approach that leverages on the identification of Lagrangian Coherent Structures (LCS) has been recently proposed by Khojasteh et al. (2021). The ETH Zurich group tackled the problem of particles reconstruction via the joint minimization of an energy function that accounts for the disparity between reconstructed particles and image recordings, while guaranteeing the sparsity of the reconstructed particles field (Lasinger et al., 2018, 2019). Some of these approaches have been comparatively assessed in the first Lagrangian Particle Tracking challenge, whose main results are discussed in Sciacchitano et al. (2021a). Applications of LPT techniques for simultaneously tracking the motion of flexible structures and of the flow tracers have been recently reported in the literature, mainly conducted within the framework of the European project HOMER (Mertens et al., 2021a, 2021b).

The knowledge of the three-dimensional information of the particles' velocities and accelerations has allowed to employ first principles (e.g. conservation of mass and momentum) and tools from Computational Fluid Dynamics (CFD) to allow the dense reconstruction of the flow properties (e.g. velocity and static pressure) in the three-dimensional measurement domain. These approaches are often categorized as Data Assimilation (DA) because of the combination between experimental data and numerical models. They range from the representation of the flow field via cubic splines, evaluated by solving an optimization problem that accounts for physical constraints (FlowFit, Gesemann et al., 2016, and its evolution) to the use of vortex methods, where the vorticity transport equation is used to retrieve a vorticity field consistent with the measured particles' velocities and accelerations (Schneiders et al., 2016, Jeon et al., 2018; Scarano et al., 2021; Jeon, 2021). A comparison of these approaches has been recently conducted by Sciacchitano et al. (2021b) considering the synthetic test case of the wall-bounded flow in the wake of a cylinder.

LPT and DA approaches have been mainly developed for the study of aerodynamic problems, focusing on the kinematics and dynamics of fluid flows in measurement domains away from solid objects or at most containing a straight wall. However, many flows of interest interact with flexible structures, giving rise to steady or unsteady fluid-structure interaction problems governed by the equilibrium of Collar's triangle of forces, namely aerodynamic, inertial and elastic forces. Only very recently, Cakir et al. (2021) explored the applicability of the VIC+ data assimilation approach in presence of generic solid boundaries via the use of the arbitrary Lagrangian-Eulerian method and of the immersed boundary treatment. Based on the above, the

purpose of the present work is to extend the assessments of LPT and DA algorithms, performed in the first Lagrangian Particle Tracking and Data Assimilation challenges (Sciacchitano et al. 2021a, 2021b), to the case where the fluid flow interacts unsteadily with a flexible structure.

2. Database description

2.1 Physical problem

A synthetic experiment is carried out which reproduces the air flow around a cylinder in ground effect, whereby the wall contains a flexible panel undergoing forced oscillations. The cylinder has a diameter D = 10 mm and is located 10 mm above the wall, at an upstream distance of 15 mm from the upstream edge of the panel. The panel has dimensions of 100 mm × 100 mm and spans the entire width of the test section; it is actuated at its midpoint via a periodic sinusoidal excitation of amplitude A = 5 mm and frequency f_{panel}=100 Hz. Two materials are considered for the panel, namely metal (Young modulus E = 70 GPa, density ρ_{metal} = 2700 kg/m^3) and rubber (hyper-elastic material with ρ_{rubber} = 950 kg/m^3, C_{10} = 1.3333 MPa and D_1 = 10^{-9} Pa^{-1}), both of thickness t = 0.5 mm. The air flow has a free-stream velocity V_∞ = 10 m/s, density of ρ = 1.22 kg/m^3 and kinematic viscosity of ν = 1.503·10^{-5} m^2/s. The boundary layer upstream of the cylinder is turbulent, with a momentum thickness Reynolds number of $Re_\theta \approx$ 4,150 measured 10 mm upstream of the cylinder's center.

2.2 Setup of the synthetic experiment and data acquisition modes

The frame of reference and measurement volume are illustrated in Figure 1. The former is defined such that the X-axis is in the streamwise direction, the Z-axis is in the wall-normal direction (oriented towards the flow), and the Y-axis is in the spanwise direction following the right-hand rule. The origin of the frame of reference is at the wall when the panel is in the undeformed configuration, 70 mm downstream of the cylinder centre. The measurement volume has a size of 100 mm × 100 mm × 30 mm (X×Y×Z), with both X and Y between –50 mm and 50 mm, and Z between 0 mm (undeformed wall location) and 30 mm.

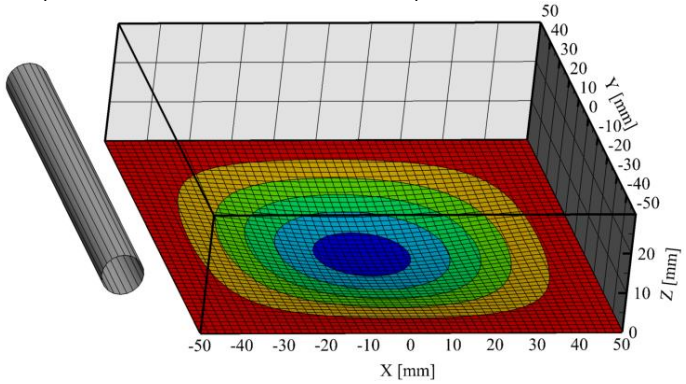

Figure 1. Illustration of the measurement domain and the system of axes.

The measurement domain is visualised with four or six synthetic cameras. Each camera has a sensor of 1920×1200 pixels, with a pixel pitch of 10 μm. The four LPT cameras are located in the XZ plane at a height of about Z = 900 mm and with viewing angles of –30°, –10°, +10° and +30° with respect to the Z-axis. The remaining two cameras are used for the Digital Image Correlation (DIC) measurements and are located in the YZ plane at Z = 900 mm and with viewing angles of -10° and +10° with respect to the Z-axis. The simulations assumed that all cameras mounted lenses with focal lengths of f = 100 mm and no optical distortions, with an aperture setting such that the particle and marker images, modelled as a Gaussian, had a diameter of $2.4\,\overline{px}$ ($\sigma = 0.6\,\overline{px}$). Based on such optical setup, the size of the back-projected pixel in the object space is $\overline{px} = 86.7\ \mu m$. Two types of setup were considered. In the *1Lambda* setup, only one light source illuminated the tracer particles and the markers on the panel, and only the four LPT cameras were employed. Instead, in the *2Lambda* setup, two light sources with two different wavelengths and optical filters were simulated: one light source illuminated the tracer particles, which were recorded by the four LPT cameras, and the other one illuminated the panel markers, which were viewed by the two DIC cameras. The markers were randomly distributed on the panel's surface at three different densities, namely low-density (*LD*) corresponding to a number of particles per pixels $ppp \approx 0.001$, medium-density (*MD*) with $ppp \approx 0.01$ and high-density with $ppp \approx 0.06$. The flow was seeded with tracer particles at two seeding densities of $ppp = 0.05$ and $ppp = 0.12$; notice that these numbers indicate the number of flow tracer particles per pixel, without accounting for the number of panel markers.

For the LPT part, three different image acquisition modes were considered, namely two-pulse (*TP*), four-pulse (*FP*) and time-resolved (*TR*). In the two-pulse acquisition, the participants were supplied with sets of single-exposure double-frame images with time separation Δt = 40 μs, acquired at a frequency f_{acq} = 2 kHz. Because of the slow motion of the panel, the participants could use any image of the set to track the markers or perform DIC. The four-pulse acquisition consisted in double-frame double-exposure sets of images; the following temporal patterns were considered, expressed in units of Δt = 40 μs: 212, 222 and 414. The convention is as follows, explained for the case 212: the first number (2) corresponds to the time separation between the two exposures of the first frame ($2\Delta t$ = 80 μs); the second number (1) is the inter-frame time separation ($1\Delta t$ = 40 μs); the third number (2) is time separation between the two exposures of the second frame ($2\Delta t$ = 80 μs). In the time-resolved acquisition, the datasets contained 501 images regularly spaced in time at a time separation of Δt = 40 μs. The images were characterized by a high level of particle polydispersity and noise, with the aim of mimicking an experimental context with a medium to low signal-to-noise ratio. The histogram of the particles' peak intensities has a peak at the grey level of 300 counts, with minimum and maximum particle intensities of 100 and 1000 counts, respectively. The distribution of the markers' peak intensity in the images was chosen as uniform, between 800 and 1000 counts. Thermal noise was added in the images and modelled as a Gaussian distribution with 100 counts mean and 40 counts standard deviation. The above-mentioned settings thus led to having around 10% of the particles with an intensity maximum smaller than the maximum level of thermal noise (see Figure 2). Photon-shot noise was also added to the images.

For the DA part, the participants were supplied with the three-dimensional distributions of tracer particles and panel markers in the physical space, and were asked to reconstruct the velocity fields and pressure distributions. The datasets comprised two different panel markers densities, namely low-density (*LD*, ppp ≈ 0.001) and medium-density (*MD*, ppp ≈ 0.01), and, for each marker density, three different tracer particles densities: *ppp* = 0.02, 0.08 and 0.16. The datasets contained sequences of 501 evenly spaced time instants at constant time separation $\Delta t = 40$ μs. Gaussian noise with standard deviation of $0.1\,\overline{px} = 8.67\ \mu m$ was added to both the particles' and makers' positions.

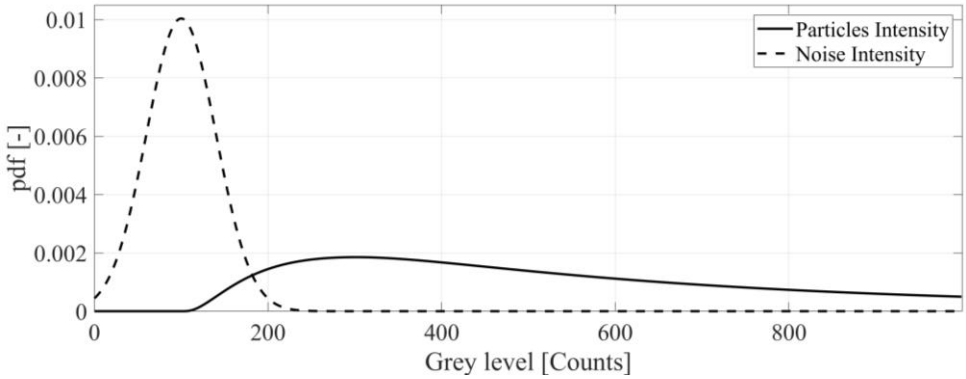

Figure 2. Probability density functions of the particles' intensities and of the thermal noise in the LPT images.

The test cases contained in the database are summarised in Table 1. Table 2 reports the average number of particles, concentration and inter-particle distance at the three *ppp* values for the DA datasets.

Table 1. List of cases present in the database. ✓ indicates that the combination of setup, marker density and *ppp* is present, ✗ indicates that the combination is not present. Each test case contains two data sets with the two panel materials, namely rubber and metal. The LPT and DIC sets contain data sets with three image acquisition modes, namely TP, FP and TR.

Setup and marker density	**LPT and DIC**		**DA**		
	0.05 *ppp*	0.12 *ppp*	0.02 *ppp*	0.08 *ppp*	0.16 *ppp*
1Lambda-LD	✓	✓	✓	✓	✓
1Lambda-MD	✓	✓	✓	✓	✓
2Lambda-MD	✓	✓	✗	✗	✗
2Lambda-HD	✓	✓	✗	✗	✗

Table 2. Average number of particles, concentration and inter-particle distance at the three *ppp* values for the DA datasets.

ppp	Avg. number of particles	Concentration [particles/mm^3]	Avg. inter-particle distance [mm]
0.02	23,181	0.08	1.46
0.08	92,261	0.31	0.92
0.16	185,597	0.62	0.73

2.3 Data analysis

The data analysis follows the same approach presented in the discussion of the main results of the Lagrangian Particle Tracking (Sciacchitano et al., 2021a) and Data Assimilation (Sciacchitano et al., 2021b) challenges. In particular, the LPT data were analysed based on the evaluation of the following parameters:

- Percentage of *correct particles*, defined as particles within 86.7 μm (or 1 $\overline{px}$) from a true particle;
- Percentage of *false particles* (or ghost), defined as particles whose distances from true particles exceed 86.7 μm (or 1 $\overline{px}$);
- Percentage of *false negatives* (or missed particle), that are true particles not associated with any reconstructed particles within 86.7 μm, or 1 $\overline{px}$, from the former;
- Errors of the following quantities (evaluated considering only the particles of the correct tracks):
    - Particles' positions (for all cases);
    - Particles' velocities (only for the FP and TR cases);
    - Particles' accelerations (only for the FP and TR cases);
    - Panel markers' positions, velocities and accelerations (for all cases).

Instead, the DA data were analysed by evaluating the errors of the panel's Z-position and surface static pressure, as well as the errors of the velocity components and static pressure in the flow field.

2.4 Participants and approaches

The data were shared within the participants of the HOMER consortium, which is composed of the German Aerospace Centre DLR, Delft University of Technology in the Netherlands, the French Aerospace Research Centre ONERA, the German University of Armed Forces in Munich UniBW, the University of Southampton in the UK, the French National Centre of Scientific Research CNRS, and the German instrumentation company LaVision GmbH.

So far, the LPT data have been processed by the DLR and LaVision research groups, whereas the DA data have been analysed only by the LaVision group. Both the DLR and LaVision groups made use of the Shake-The-Box (STB, Schanz et al., 2016) Lagrangian Particle Tracking algorithm and of its advances for two-pulse and multi-pulse data processing (Novara et al., 2019). The differences between the DLR and the LaVision implementations were mainly in the number of iterations for the particles' triangulation and subsequent shaking and the algorithm used for fitting the particles' trajectories (TrackFit with Cubic B-spline for DLR, second order polynomial

for LaVision). The LaVision DA results were obtained via the VIC#-FSI algorithm based on the Vortex-in-Cell framework (Jeon, 2021).

3. Results

3.1 Lagrangian Particle Tracking

3.1.1. Time-Resolved acquisition

The results for the metal plate, middle marker density and *2Lambda* setup are presented here. Figure 3 illustrates the distribution of the ground-truth tracer particles in a 2 mm thick slab centred on the median plane Y = 0 mm. The particles are colour-coded by the streamwise velocity component. The flow field is clearly turbulent, with large velocity fluctuations ascribed both to the turbulent nature of the boundary layer and to the Kármán wake of the cylinder.

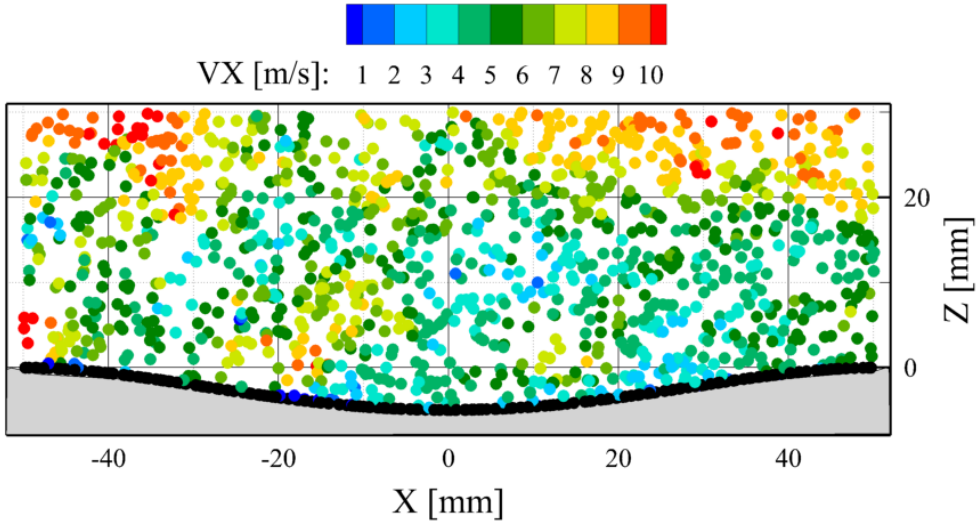

Figure 3. Ground truth particles distribution in a slab –1 mm < Y < 1 mm, colour-coded by streamwise velocity; panel markers are illustrated in black. Metal plate, case *MD*, *2Lambda*, *ppp* = 0.05.

The visual inspection of the true and reconstructed particles (Figure 4) shows that the DLR algorithm is capable of reconstructing the great majority of the particles even at the largest *ppp* of 0.12, with very few ghost particles. For the LaVision algorithm, instead, more missed particles are noticed already at the lowest *ppp* of 0.05. The above is confirmed by the quantitative results summarised in Table 3: for the DLR algorithm, more than 95% of the particles are correctly reconstructed at both *ppp* values, with a negligible percentage of ghost particles (below 1%). Conversely, for the LaVision algorithm, the percentages of correctly reconstructed particles are about 83% and 71% at *ppp* = 0.05 and 0.12, respectively. At both *ppp* values, the percentages of ghost particles remain between 1% and 2%.

The root-mean-square (RMS) errors on position, velocity and acceleration are also reported in Table 3. Let us first focus on the position error. From the analysis of the results, it is evident that the errors in the X and Y position are comparable, whereas those in the Z-position are two to three times larger. This result is attributed to the fact that the cameras are positioned on top of the measurement domain (towards positive Z values), hence the Z-direction is close to the viewing direction of the cameras. Also, it is noticed that the increase of the *ppp* value from 0.05 to 0.12 causes only a moderate increase of the error level of about 10%. Finally, the errors obtained with the LaVision algorithm are twice as large as those of the DLR algorithm. When looking at the velocity errors, similar conclusions can be drawn: the errors of VX and VY are similar to each other and smaller than those on VZ; the LaVision algorithm yields larger error values. Overall, the velocity errors are between 0.5% and 2.5% of the free-stream velocity, values that are representative of a high-quality experiment, despite the important noise level and particle polydispersity. Instead, the acceleration errors range between 8% and 30% of the reference acceleration V_∞^2/D, which indicates that the accurate evaluation of the Lagrangian acceleration is still an open challenge. As for the position and the velocity, also for the acceleration the errors are larger for the Z-component than for the X- and Y- components.

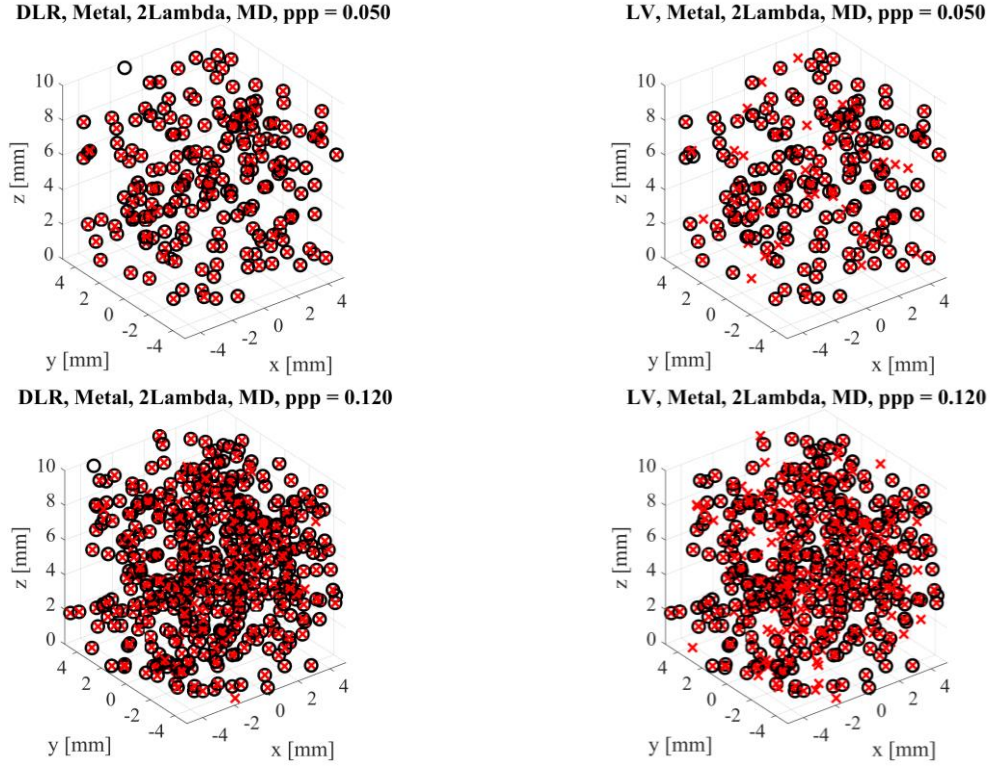

Figure 4. Visualization of the true particles (red crosses) and reconstructed particles (black circles) in a sub-volume of the entire measurement domain. Left: DLR result; Right: LaVision result. Top row: *ppp* = 0.05; bottom row: *ppp* = 0.12. Results for the metal plate, middle marker density, 2-Lambda setup, for the time-resolved (TR) image acquisition.

Table 3. Percentages of correctly reconstructed particles (true positives), false positives and false negatives, and position, velocity and acceleration RMS errors of the reconstructed particles. All results refer to the intermediate (fitted) time instant. Results for the metal plate, middle marker density, *2Lambda* setup, for the time-resolved (TR) image acquisition. For the percentage values on velocity and acceleration errors, the reference velocity is V_∞ = 10 m/s, whereas the reference acceleration is V_∞^2/D = 10,000 m/s^2.

	DLR		**LaVision**	
	***ppp* = 0.05**	***ppp* = 0.12**	***ppp* = 0.05**	***ppp* = 0.12**
True positives	97.8%	95.9%	83.3%	71.1%
False positives (ghosts)	0.1%	0.9%	1.4%	1.7%
False negatives (missed)	2.2%	4.1%	16.7%	28.9%
RMS error on X μm ($\overline{px}$)	4.1 (0.05)	4.6 (0.05)	9.6 (0.11)	10.4 (0.12)
RMS error on Y μm ($\overline{px}$)	3.8 (0.04)	4.2 (0.05)	9.7 (0.11)	10.4 (0.12)
RMS error on Z μm ($\overline{px}$)	9.5 (0.11)	10.6 (0.12)	16.1 (0.19)	18.0 (0.21)
RMS error on VX m/s (%)	0.052 (0.5%)	0.059 (0.6%)	0.181 (1.8%)	0.179 (1.8%)
RMS error on VY m/s (%)	0.051 (0.5%)	0.056 (0.6%)	0.186 (1.9%)	0.185 (1.8%)
RMS error on VZ m/s (%)	0.095 (0.9%)	0.109 (1.1%)	0.213 (2.1%)	0.250 (2.5%)
RMS error on AX m/s^2 (%)	830 (8.3%)	921 (9.2%)	1376 (13.8%)	1748 (17.5%)
RMS error on AY m/s^2 (%)	775 (7.8%)	908 (9.1%)	1448 (14.5%)	1668 (16.7%)
RMS error on AZ m/s^2 (%)	1245 (12.5%)	1398 (14.0%)	2052 (20.5%)	3172 (31.7%)

The probability distributions of the particles' positional errors are shown in Figure 5, for the streamwise (X) and wall-normal (Z) components. The error distributions in the spanwise direction Y are similar to those in the streamwise direction X, and therefore are not reported. All error distributions are centred on zero, indicating that only random errors are present, whereas the systematic errors are negligible. As discussed before, the position errors in the streamwise (X) directions are 2 to 3 times lower than the corresponding errors in the wall-normal (Z) direction, resulting in narrower error distributions. Also, the differences in the results between the two *ppp* values (0.05 and 0.12, respectively) are small compared the differences between the algorithm.

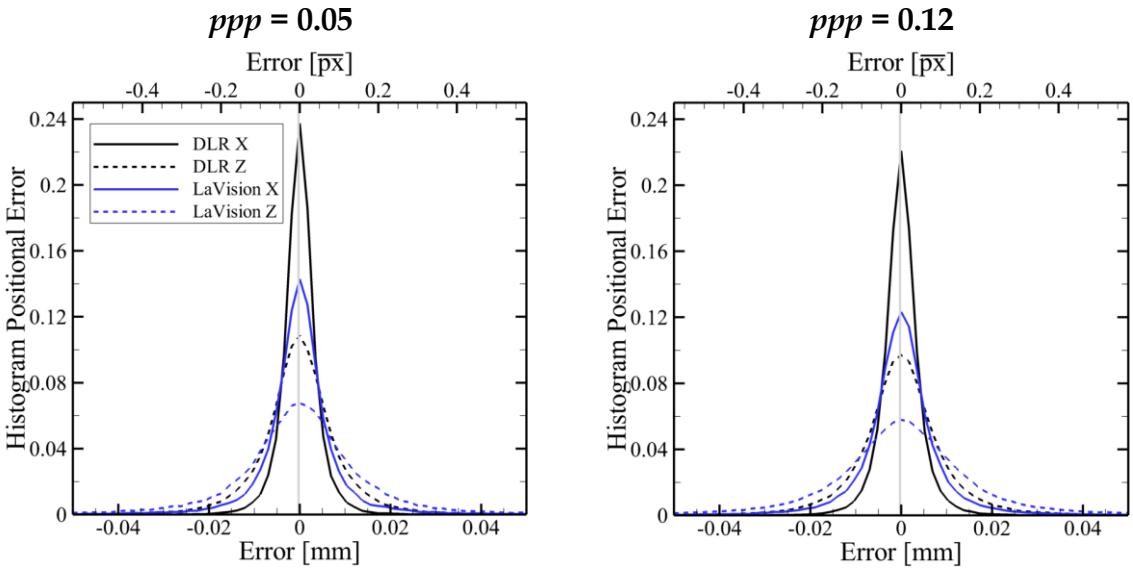

Figure 5. Histograms of the errors of the particles' positions, for *ppp* = 0.05 (left) and *ppp* = 0.12 (right).

Figure 6 illustrates the comparison between the measured and the ground truth particles velocities and accelerations (only the Z-component is shown for sake of conciseness). For perfect particles reconstructions, the scatter plots in Figure 6 should align along straight lines having unitary slope and passing through the origin, because the measured velocity and accelerations should coincide with the true ones. For the DLR algorithm, both velocity and acceleration are reconstructed with high accuracy, and indeed the scatter plots align along a straight line with unitary slope, with very little spread especially for the velocity. Even large accelerations above 20,000 m/s^2 are captured mostly correctly. Instead, the LaVision distributions (right column) are broader, indicating larger measurement errors. In particular, the acceleration plot shows that large errors O(10,000 m/s^2) are present even for particles featuring close-to-null accelerations.

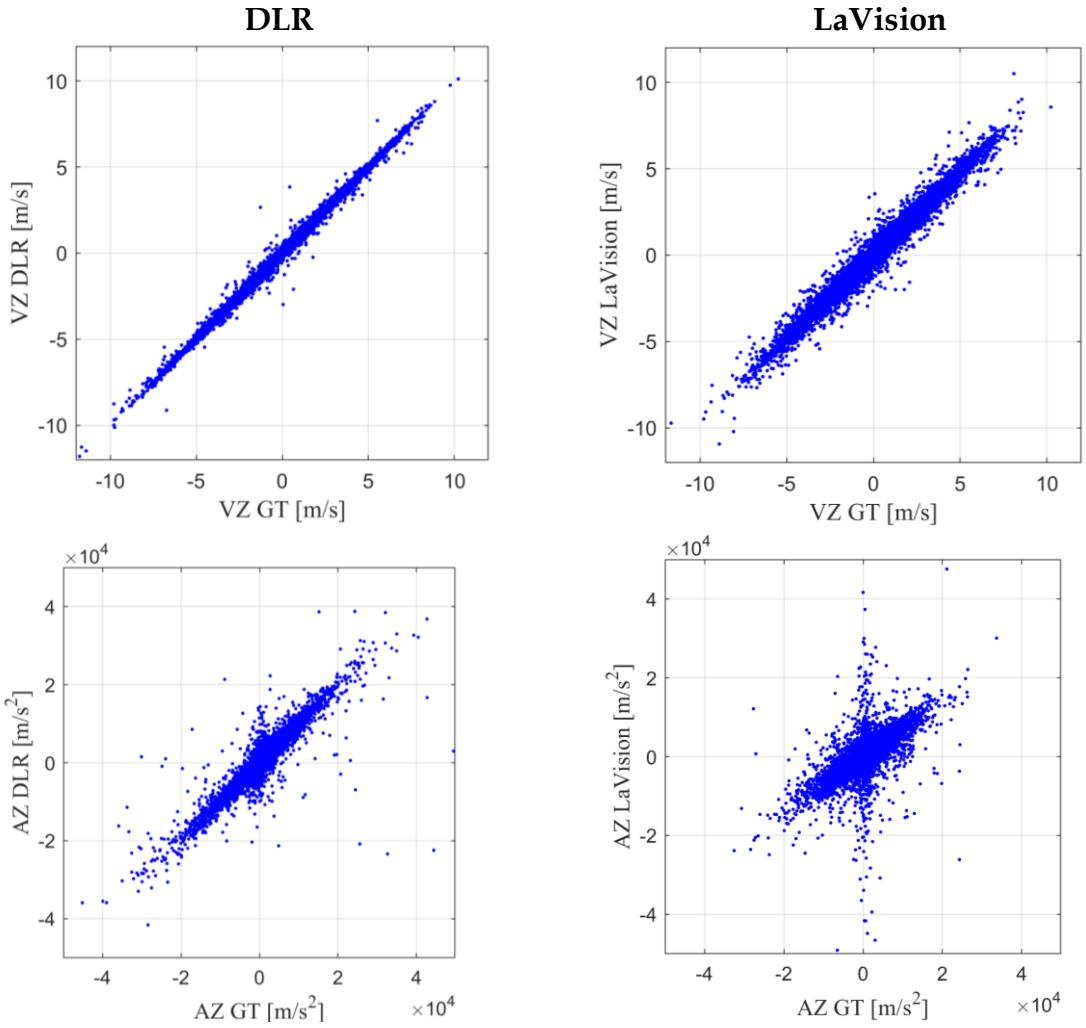

Figure 6. Measured particles velocities (top row) and accelerations (bottom row) as functions of the ground truth values. Only the Z-components are shown. Left column: DLR evaluation; right column: LaVision evaluation. Results for metal plate, case *MD*, *2Lambda*, *ppp* = 0.05, TR acquisition.

Figure 7 compares the panel's Z-position (left), velocity (middle) and acceleration (right) between ground truth (top row) and those reconstructed by the DLR group (bottom row) for the metal plate, *MD* case, *2Lambda*, *ppp* = 0.05. The panel is deflected downwards, with its centre located at Z = –5 mm with velocity VZ= –0.35 m/s and acceleration AZ = 1931 m/s². The DLR algorithm correctly reconstructs the totality of the markers, with no ghosts. From visual inspection, the panel's position, velocity and acceleration are reconstructed with very high accuracy, with no noticeable errors. This is confirmed by the quantitative results of Table 4, whereby the RMS errors on Z-position, velocity and acceleration are indeed a small fraction (below 1%) of the reference values.

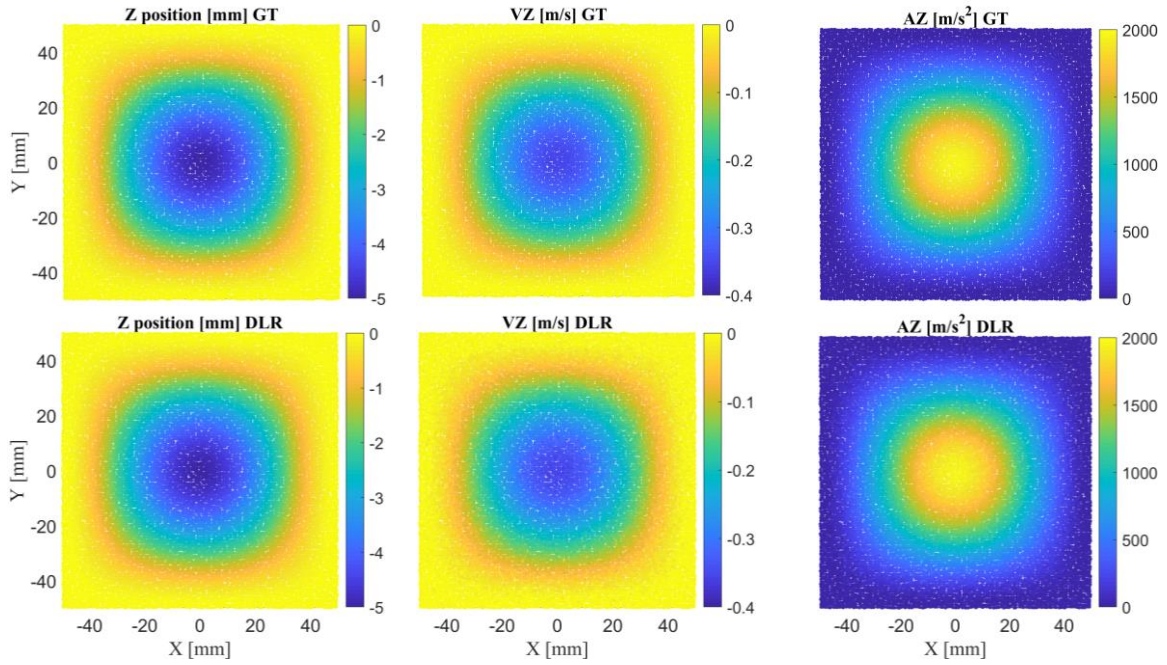

Figure 7. Z-components of the panel's position in mm (left), velocity in m/s (middle) and acceleration in m/s² (right). Comparison between ground truth (top row) and DLR evaluation for the metal plate, case *MD*, *2Lambda*, *ppp* = 0.05, TR acquisition.

Table 4. Root-mean-square errors on the fitted Z-position, VZ and AZ of the panel's markers as evaluated by the DLR group for the metal plate, case *MD*, *2Lambda*, *ppp* = 0.05 and 0.12, TR acquisition. Percentages are with respect to the maximum panel's displacement (5 mm), velocity (3.14 m/s) and acceleration (1974 m/s²).

	***ppp* = 0.05**	***ppp* = 0.12**
RMS error on Z µm (%)	2.6 (0.05%)	2.7 (0.05%)
RMS error on VZ m/s (%)	0.006 (0.2%)	0.006 (0.2%)
RMS error on AZ m/s² (%)	18.8 (1%)	18.7 (1%)

3.1.2. Two-Pulse acquisition

In this section we present the results for the metal plate, middle marker density and *2Lambda* setup for the two-pulse (TP) image acquisition. Figure 8 illustrates the spatial distributions of the true and reconstructed particles in a sub-volume of the entire measurement domains, for the DLR and LaVision algorithms for *ppp* = 0.05. As in the time-resolved case, the majority of the particles are correctly reconstructed, with smaller percentages of missed and ghost particles. As it can be seen in the results of Table 5, for both the DLR and LaVision algorithms, the percentages of correctly reconstructed particles decrease with increasing *ppp*, whereas the percentages of ghost particles increases. The latter remains below 1% with the DLR algorithm, whereas it exceeds 5% with the LaVision algorithm at the highest *ppp*. Overall, the DLR

algorithms yields the most accurate particle reconstruction, with over 80% of true positives at *ppp* = 0.12; conversely, the LaVision algorithms returns only 51% true positives at that seeding density. These values are significantly lower than those found in the time-resolved image acquisition (96% and 71%, respectively), clearly indicating that the presence of temporal information enhances the quality of the particles' reconstructions.

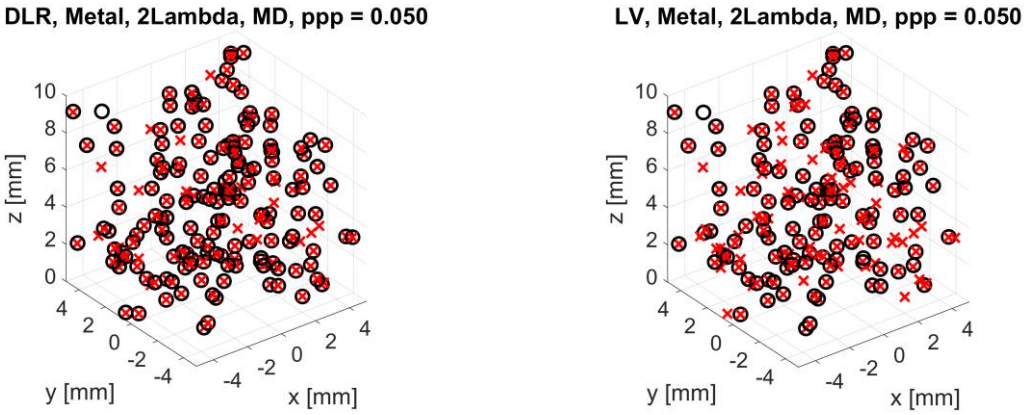

Figure 8. Visualization of the true particles (red crosses) and reconstructed particles (black circles) in a sub-volume of the entire measurement domain. Left: DLR result; Right: LaVision result. Results for the metal plate, middle marker density, 2*Lambda* setup, *ppp* = 0.05, for the two-pulse (TP) image acquisition.

Table 5. Percentages of correctly reconstructed particles (true positives), false positives and false negatives, and positional RMS errors of the reconstructed particles. Results for the metal plate, middle marker density, 2*Lambda* setup, for the two-pulse (TP) image acquisition, considering both time instants.

	DLR		**LaVision**	
	***ppp* = 0.05**	***ppp* = 0.12**	***ppp* = 0.05**	***ppp* = 0.12**
True positives	89.1%	82.2%	75.0%	51.1%
False positives (ghosts)	0.3%	0.6%	1.2%	5.6%
False negatives (missed)	10.9%	17.8%	25.0%	48.9%
RMS error on X µm ($\overline{px}$)	7.5 (0.09)	8.8 (0.10)	9.7 (0.11)	12.1 (0.14)
RMS error on Y µm ($\overline{px}$)	6.8 (0.08)	8.0 (0.09)	8.9 (0.10)	11.3 (0.13)
RMS error on Z µm ($\overline{px}$)	18.5 (0.21)	21.3 (0.23)	23.5 (0.27)	28.0 (0.32)

Table 5 also reports the root-mean-square (RMS) errors of the reconstructed particles positions. The errors in the X- and Y-positions are comparable, and are typically below 10 µm or 0.11 $\overline{px}$. Conversely, the errors on the Z-position, corresponding to the cameras viewing direction, are close to 20 µm for the DLR algorithm, or even approaching 30 µm for the LaVision algorithm.

Between *ppp* = 0.05 and *ppp* = 0.12, the positional error increases by about 10-20%. Comparing the two algorithms, the DLR one outperforms the LaVision analysis, yielding lower errors.
The histograms of the positional errors in the streamwise (X) and wall-normal (Z) directions are shown in Figure 9. From the figure, it is clear that the error distributions are centred on zero, indicating that no systematic error is present. As in the TR case, the Z-error distribution is significantly broader than the X-error distribution, which is attributed to the viewing direction of the cameras. The histograms also confirm the slight error increase when increasing the seeding density from *ppp* = 0.05 to *ppp* = 0.12, thus resulting in broader error distributions.

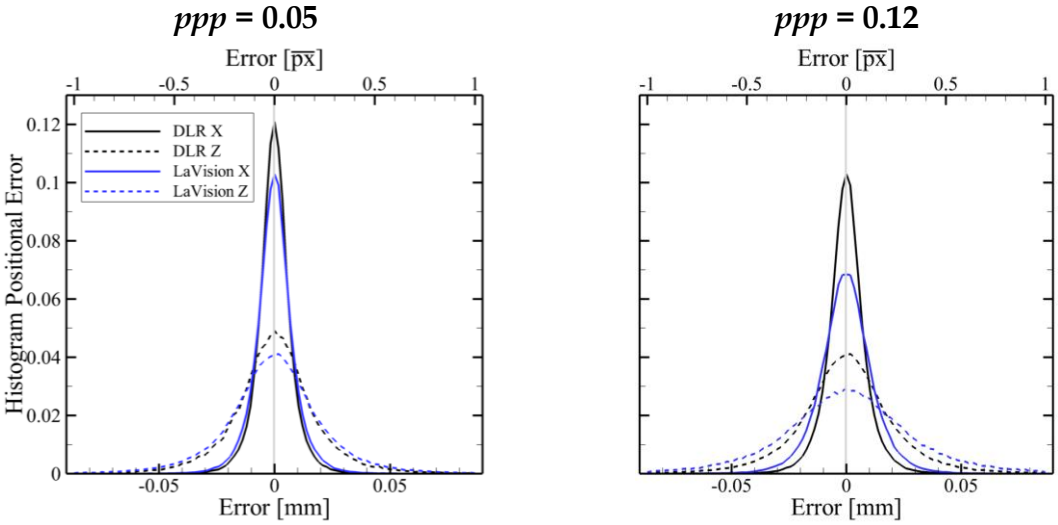

Figure 9. Histogram of the positional error in the streamwise (X) and wall-normal (Z) directions for *ppp* = 0.05 (left) and *ppp* = 0.12 (right). Results for the metal plate, middle marker density, 2*Lambda* setup, for the two-pulse (TP) image acquisition, considering both time instants.

3.1.3 Four-Pulse acquisition

Also for the four-pulse acquisition, the results for the metal plate, middle marker density, *2Lambda* setup are discussed, considering the time sequence 212. The particles' distribution of Figure 10 shows that, as for the TR and TP cases, the majority of the particles are correctly reconstructed, with a negligible amount of ghost particles. From the figure, the amount of missed particles seems larger for the LaVision algorithm (Figure 10-right). This result is confirmed by the results of the particles reconstruction analysis reported in Table 6, whereby the DLR algorithm returns 86% and 77% correctly reconstructed particles at the two *ppp* values, whereas for the LaVision algorithm the percentages of true positives are 66% and 54%, respectively. For the DLR algorithm, the amount of ghost particles is negligible (below 0.2% of

the total number of particles), which instead increases up to 2.4% with the LaVision implementation.

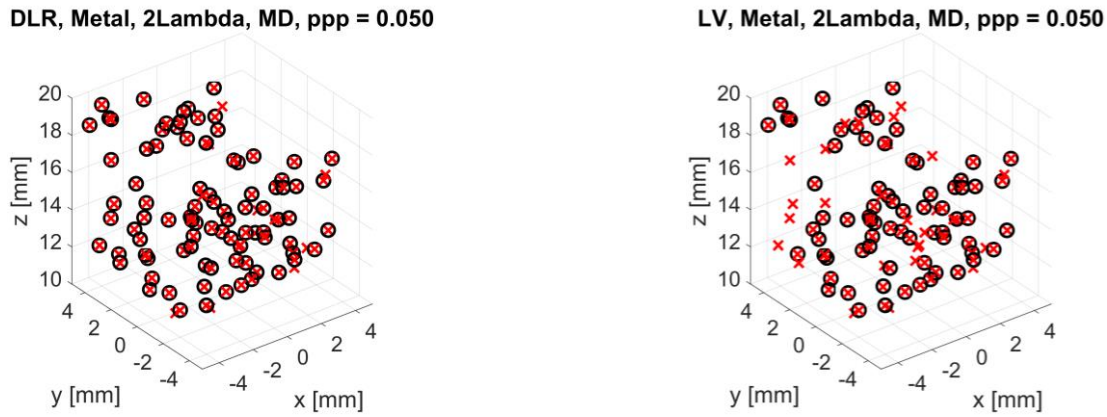

Figure 10. Representation of the true particles (red crosses) and reconstructed particles (black circles) in a sub-volume of the entire measurement domain. Left: DLR result; Right: LaVision result. Results for the metal plate, middle marker density, 2*Lambda* setup, *ppp* = 0.05, for the four-pulse (FP) image acquisition with time scheme 212.

The positional RMS errors, also summarized in Table 5, exhibit values about 30-40% lower than those found in the TP case, namely between 5 μm and 15 μm for the DLR algorithm, and up to 20 μm for the LaVision algorithm. Also in this case, the errors in the Z-direction (i.e. the cameras viewing direction) are more than twice as large as the errors in the X- and Y-directions. Similarly, the velocity errors are smaller in the X- and Y-directions, typically between 0.6% and 1.1% of the free-stream velocity, and larger in the Z-direction, up to 1.9% of V_∞. The acceleration errors range between 15% and 54% of the reference acceleration V_∞^2/D. The acceleration errors are two to three times larger than those obtained in the TR acquisition, which is ascribed both to the lower number of samples (only 4) along a track and the lower distance travelled by a particle along each track. As in the TR and TP cases, also in the FP case the DLR algorithm yields lower errors than the LaVision algorithm.

The histograms of the position errors, illustrated in Figure 11, confirm what discussed above. The errors on the Z components are two to three times larger than those on the X and Y components (the latter are not shown for sake of clarity). The increase of seeding concentration from *ppp* = 0.05 to *ppp* = 0.12 yields a slight increase of the measurement errors. The particles position the errors are rather small (typically within 0.2 $\overline{px}$), centred at zero and rather symmetrical, indicating the absence of large systematic errors.

Table 6. Percentages of correctly reconstructed particles (true positives), false positives and false negatives, and position, velocity and acceleration RMS errors of the reconstructed particles at the intermediate time instant t_M. Results for the metal plate, middle marker density, *2Lambda* setup, for the two-pulse (FP) image acquisition with time scheme 212. For the percentage values on velocity and acceleration errors, the reference velocity is V_∞ = 10 m/s, whereas the reference acceleration is V_∞^2/D = 10,000 m/s².

	DLR		**LaVision**	
	***ppp* = 0.05**	***ppp* = 0.12**	***ppp* = 0.05**	***ppp* = 0.12**
True positives	86.0%	76.7%	65.6%	54.0%
False positives (ghosts)	0.1%	0.2%	0.3%	2.4%
False negatives (missed)	14.0%	23.3%	34.4%	46.0%
RMS error on X µm ($\overline{px}$)	5.4 (0.06)	6.3 (0.07)	6.7 (0.08)	8.2 (0.09)
RMS error on Y µm ($\overline{px}$)	4.9 (0.06)	5.8 (0.07)	6.5 (0.06)	7.8 (0.09)
RMS error on Z µm ($\overline{px}$)	13.3 (0.15)	15.4 (0.18)	16.5 (0.19)	19.8 (0.23)
RMS error on VX m/s (%)	0.06 (0.6%)	0.07 (0.7%)	0.10 (1.0%)	0.11 (1.1%)
RMS error on VY m/s (%)	0.06 (0.6%)	0.07 (0.7%)	0.09 (0.9%)	0.09 (0.9%)
RMS error on VZ m/s (%)	0.13 (1.3%)	0.15 (1.5%)	0.16 (1.6%)	0.19 (1.9%)
RMS error on AX m/s² (%)	1510 (15.1%)	1741 (17.4%)	1857 (18.6%)	2259 (22.6%)
RMS error on AY m/s² (%)	1370 (13.7%)	1586 (15.9%)	1723 (17.2%)	2101 (21.0%)
RMS error on AZ m/s² (%)	3741 (37.4%)	4273 (42. 7%)	4508 (45.1%)	5405 (54.1%)

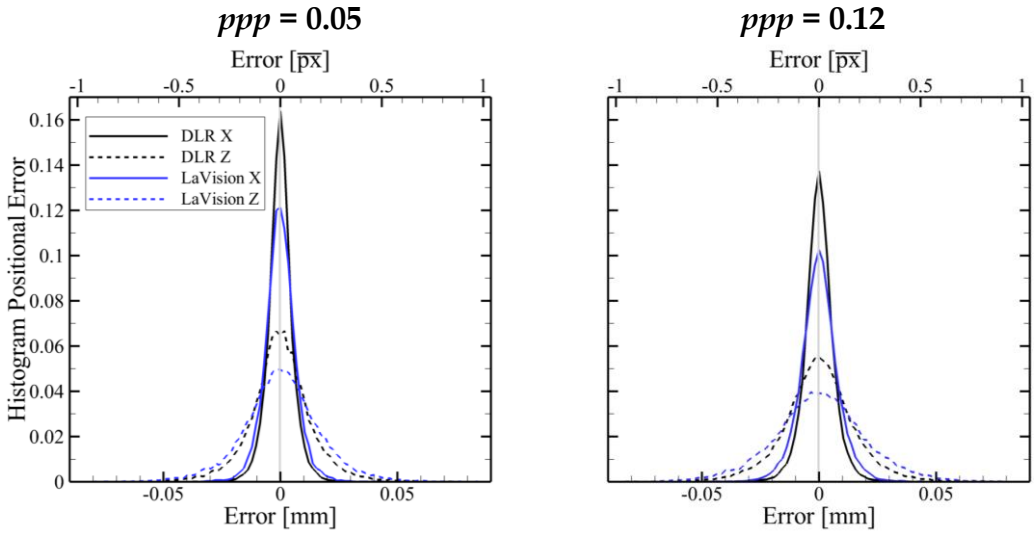

Figure 11. Histograms of the position error for *ppp* = 0.05 (left column) and *ppp* = 0.12 (right column). Results for the metal plate, middle marker density, *2Lambda* setup, for the four-pulse (FP) image acquisition with time scheme 212.

In Figure 12, the comparisons between ground truth and measured velocities and accelerations are illustrated for the case *ppp* = 0.05. As explained already for the discussion of the TR results, perfect particles reconstruction should return scatter plots aligned along a straight line with unitary slope, meaning that measured and ground truth values coincide. This is indeed what happens for the velocity, with a typical spread within 0.1 m/s or 1% of V_∞. Instead, the distributions are much wider for the acceleration plots, with errors O(10,000 m/s^2) or 100% of the reference acceleration V_∞^2/D even for relatively low true accelerations.

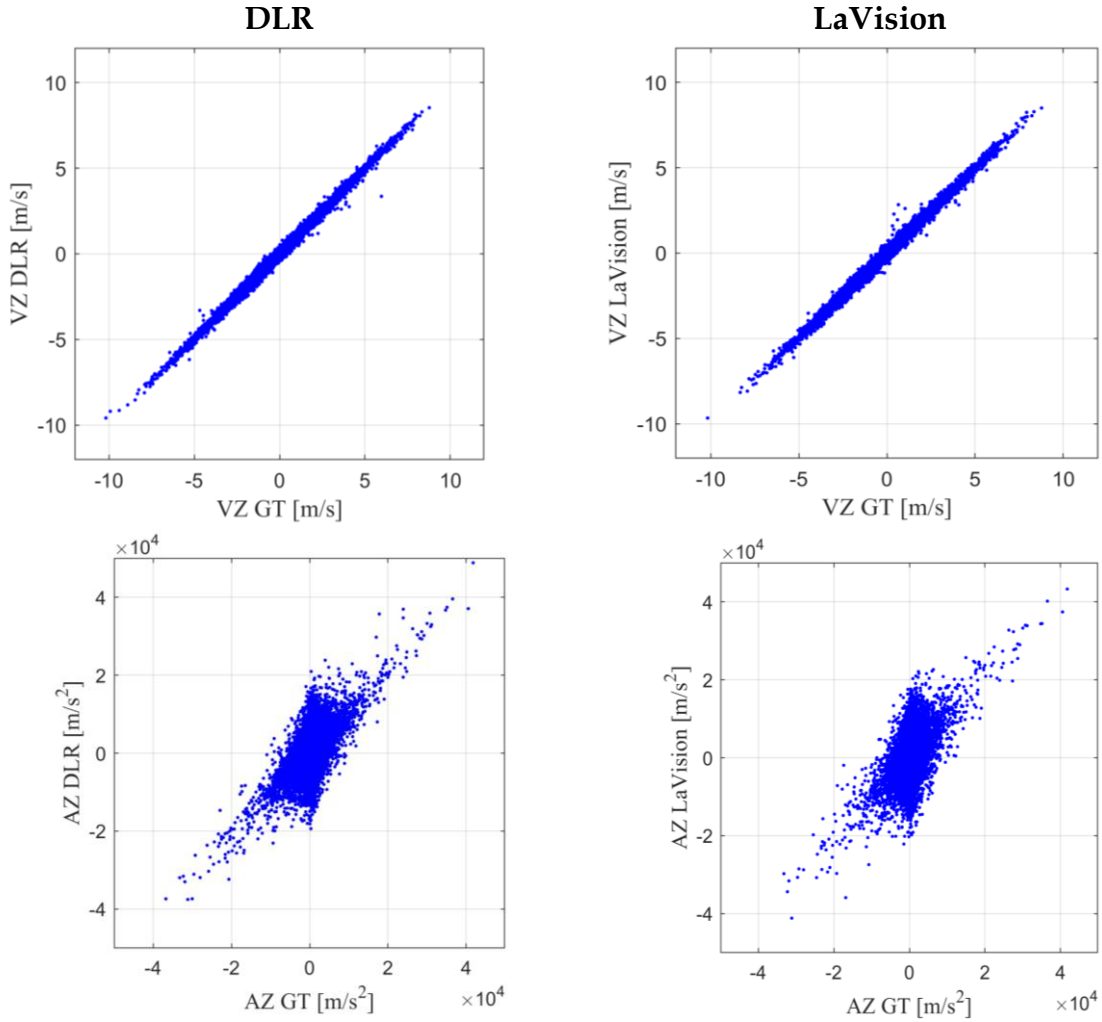

Figure 12. Measured particles velocities (top row) and accelerations (bottom row) as functions of the ground truth values. Only the Z-components are shown. Left column: DLR result; right column: LaVision evaluation. Results for metal plate, case *MD*, *2Lambda*, *ppp* = 0.05, four-pulse (FP) image acquisition with time scheme 212.

3.2. Data Assimilation

The data assimilation results of the case metal plate, *LD* case, are discussed here, for the three *ppp* values of 0.02, 0.08 and 0.16. In Figure 13, we illustrate the streamwise velocity component in the median plane (Y = 0 mm). The presence of a vertical (wall-normal) velocity gradient is evident, where the higher velocities above the free-stream value are found in the top of the measurement domain, whereas the velocity decreases to zero at the wall. The flow is clearly turbulent, with large fluctuations attributed not only to the turbulent boundary layer, but also to the Kármán vortex street in the wake of the cylinder. The LaVision 3D result at *ppp* = 0.02 (Figure 13-middle) reproduces the main flow features of the ground-truth velocity field (Figure 13-top), although with an evident spatial modulation. As expected, when the *ppp* is increased to 0.16 (Figure 13-bottom), the turbulent flow structures are reproduced with higher accuracy.

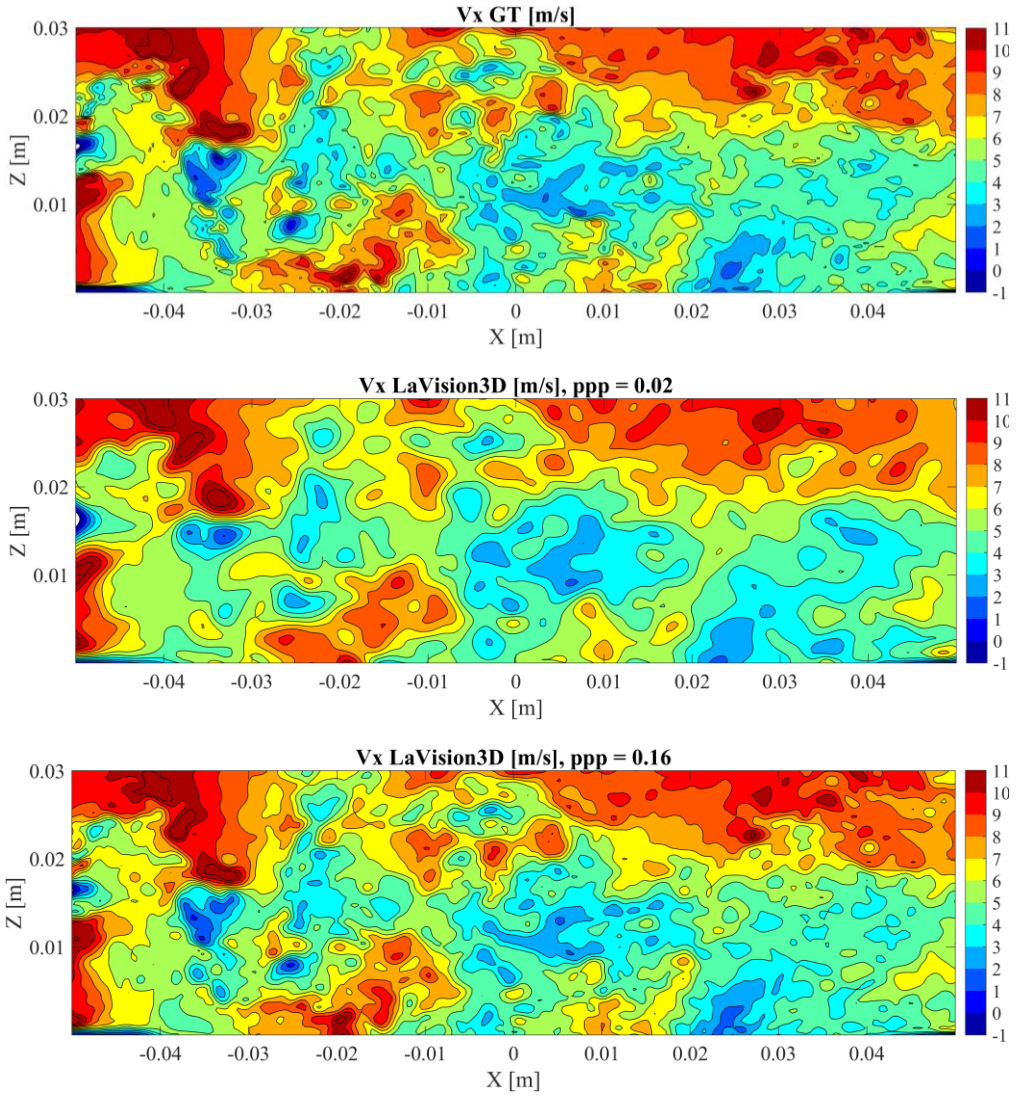

Figure 13. Comparison of contours of the streamwise velocity component in m/s at the median plane Y = 0 mm. Top: ground-truth flow field; middle: LaVision 3D result at *ppp* = 0.02; bottom: LaVision 3D result at *ppp* = 0.16.

When looking at the static pressure contour at the median plane (Figure 14), relatively high pressure is found at the location of the panel's centre (X = 0), from which the pressure decreases radially. The LaVision3D algorithm correctly reproduces this trend both at the lowest (Figure 14-middle) and highest (Figure 14-bottom) *ppp* values, with no significant bias error. However, some spatial modulation effects are noticed, as it can be seen by the low pressure structure at -0.04 m < X < -0.03 m, whose peak value is attenuated at both *ppp*'s.

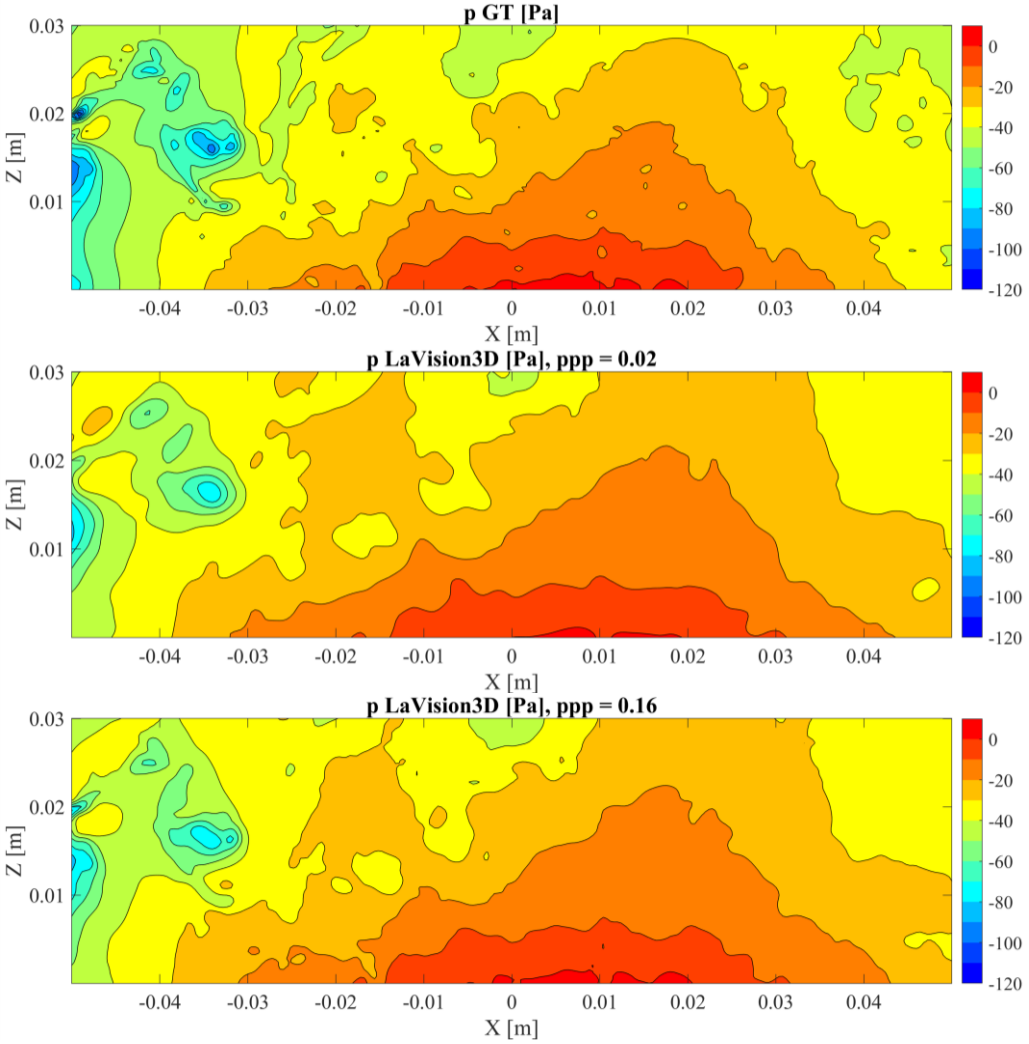

Figure 14. Comparisons of contours of the static pressure in Pa at the median plane Y = 0 mm. Top: ground-truth flow field; middle: LaVision 3D result at *ppp* = 0.02; bottom: LaVision 3D result at *ppp* = 0.16.

Figure 15 summarises the mean bias and random errors of the velocity magnitude (left) and static pressure (right) for the LaVision 3D and 4D algorithms at the three *ppp* values. As expected, the errors decrease with increasing *ppp*, which is ascribed to the ability to resolve smaller length scales in the flow when the seeding concentration is higher. Also, especially at the higher *ppp*, the use of the temporal information in the data assimilation algorithm (LaVision 4D) enhances the accuracy of the results, leading to smaller errors. For the velocity, the mean bias

errors are within 0.1 m/s or 1% of the free-stream velocity, whereas the random errors decrease from about 1 m/s (10% V_∞) at the lowest *ppp* to below 0.5 m/s (5% V_∞) at the highest *ppp*. For the static pressure, instead, the mean bias error component (4 to 8 Pa, 6.6% and 13% of q_∞) is larger than the random error component, which decreases from 4 to 2 Pa with increasing *ppp*.

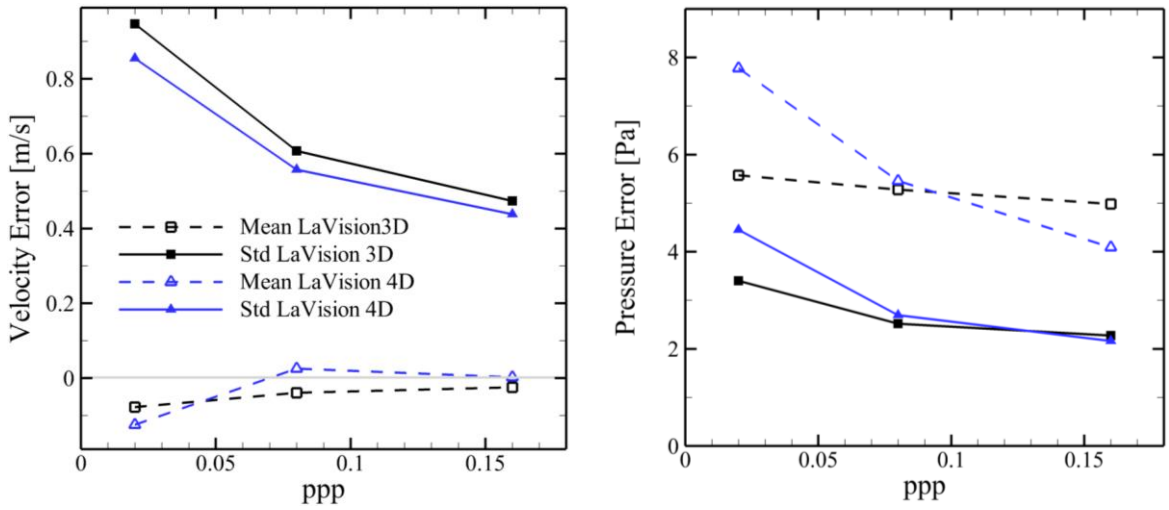

Figure 15. Mean bias and random (std) error of the velocity magnitude (left) and of the static pressure (right) in the flow field, as a function of the *ppp*. The symbol keys apply to both plots.

From the analysis of the power spectra of the wall-normal velocity component VZ, illustrated in Figure 16, the different accuracies of the velocity reconstructions at different *ppp* values emerge. As expected, the power spectra from the LaVision 3D and LaVision 4D algorithms agree with the ground truth spectrum at the lowest wave numbers (larger wave lengths λ). Instead, at higher wave numbers, the reconstructed flow fields strongly modulate the velocity fluctuations, resulting in lower values of the power spectra. In particular, at the lowest *ppp* of 0.02, the measured spectra start departing from the ground truth one already before $k \sim 200\ m^{-1}$ ($\lambda \sim 5$ mm), independently of the algorithm used (LaVision 3D or LaVision 4D). Instead, at the higher *ppp* values, the measured spectra follow the ground truth one up to $k \sim 300\ m^{-1}$ ($\lambda \sim 3$ mm) at *ppp* = 0.08 and $k \sim 360\ m^{-1}$ ($\lambda \sim 2.8$ mm) at *ppp* = 0.16, hence enabling to resolve accurately flow length scales as small as 1/3 of the cylinder's diameter or four times the inter-particle distance.

Figure 17 shows the ground truth panel's position and surface pressure (left column) in comparison with the reconstructed values from the LaVision 3D algorithm at *ppp* = 0.02 (right column). At the considered time instant, the panel is deflected downwards reaching $Z = -4.75$ mm at its centre. The panel's position is reconstructed with very high accuracy, with minor differences with respect to the true position, mainly at the panel's edges.

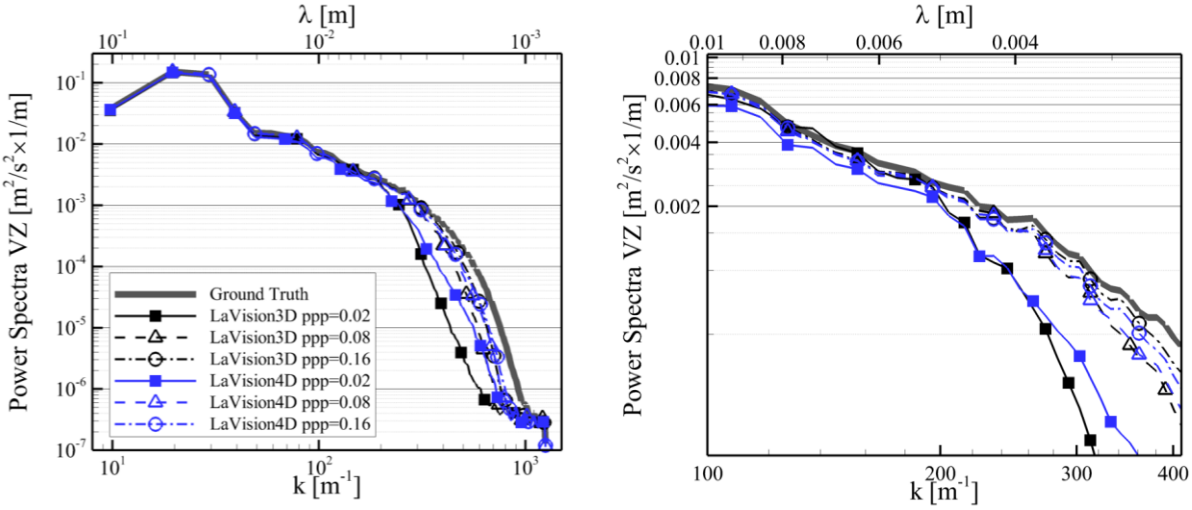

Figure 16. Power spectra of the wall-normal velocity component VZ. Left: entire spectra; right: detail for wave numbers between 100 and 410 m^{-1}. The symbol keys apply to both plots.

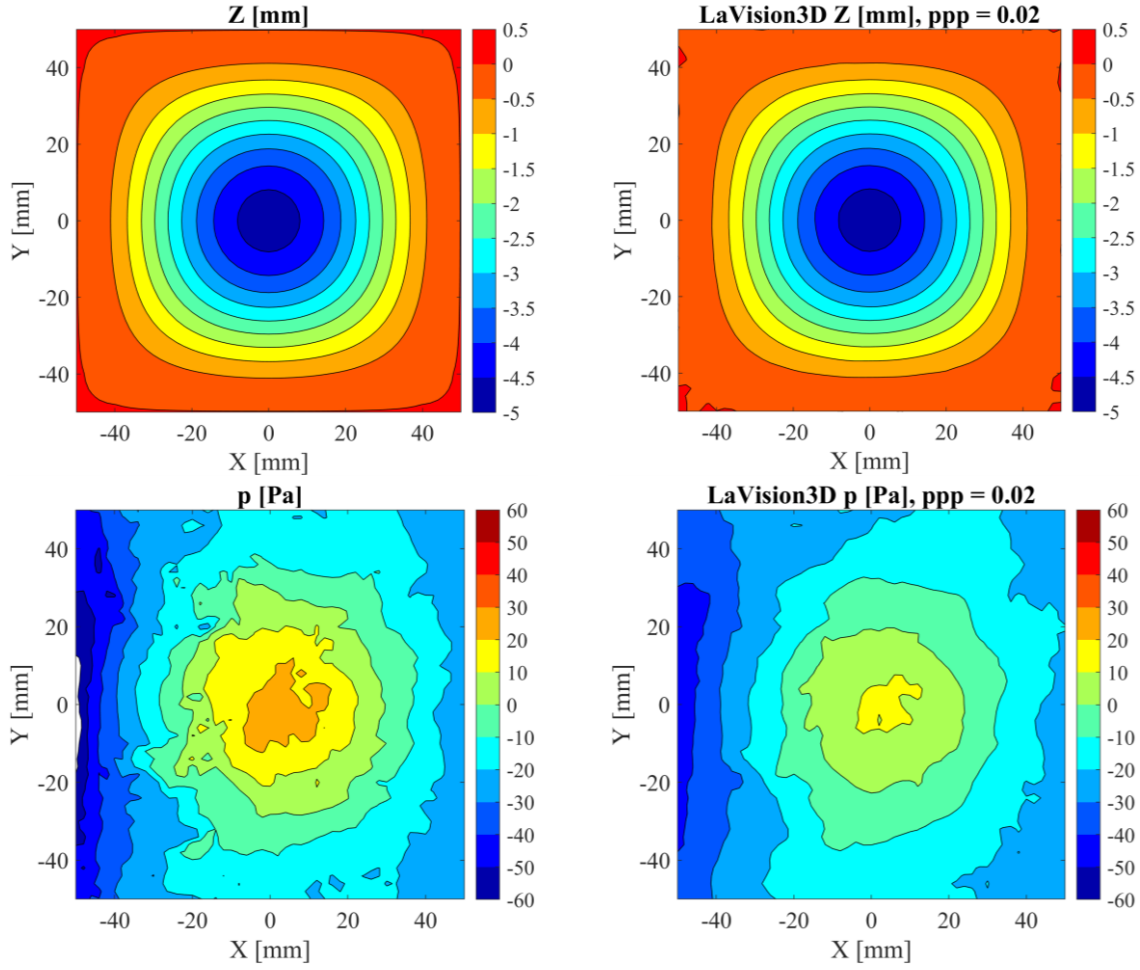

Figure 17. Left column: ground truth panel's Z-position (top) and surface pressure (bottom). Right column: panel's Z-position (top) and surface pressure (bottom) reconstructed with the LaVision 3D algorithm at *ppp* = 0.02.

The surface pressure is the minimum towards the upstream edge the panel (X < –40 mm) and reaches its maximum value p_{max} = 23 Pa at the panel's centre due to the flow deceleration caused by the panel's deflection. The reconstructed surface pressure field (Figure 17 bottom-right) reproduces correctly the trend of the ground truth surface pressure; however, the magnitudes of both the minimum and the maximum pressure values are underestimated by over 10 Pa.

A quantitative analysis of the mean bias and random errors of the panel's position and surface pressure are reported in Figure 18, considering the LaVision 3D and LaVision 4D algorithms and the three *ppp* values. The position errors (Figure 18-left) are independent of the *ppp* and the data assimilation algorithm, and attain values of –5 μm and 5 μm for the mean bias and random components, respectively, which correspond to 0.1% of the panel's maximum deflection. Such a behaviour is quite logical as the marker density is the same throughout, but also indicates that the accuracy of marker detection was not affected by the increase in particle density. Also for the surface pressure (Figure 18-right), the results obtained with the two algorithms are rather similar. The increase of *ppp* yields a decrease of the random errors from 8 Pa to 4 Pa, whereas the mean bias error slightly increases in magnitude, especially for the LaVision 4D algorithm, reaching –4 Pa at the highest *ppp*.

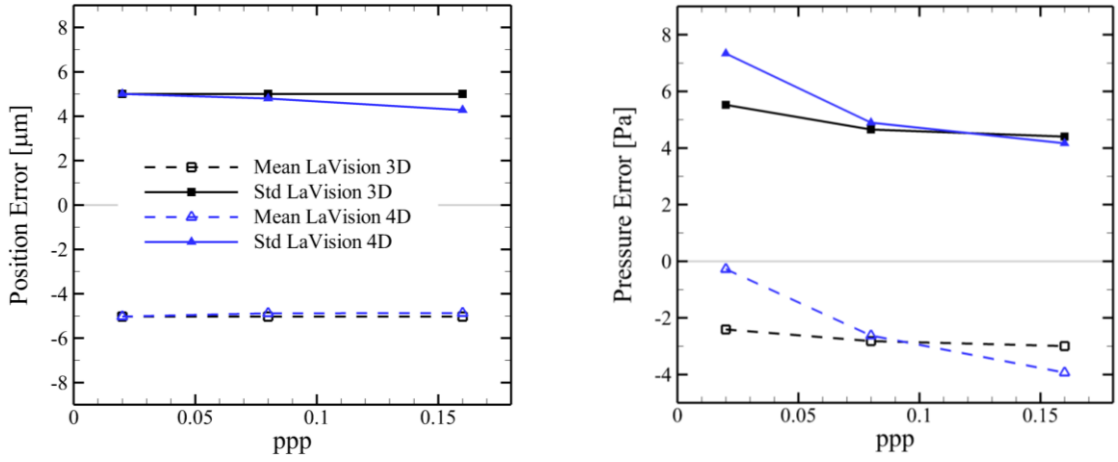

Figure 18. Mean bias and random (std) error of the reconstructed Z-position of the panel (left) and of the surface static pressure on the panel (right), as a function of the *ppp*. The symbol keys apply to both plots.

4. Conclusions

A benchmark synthetic database is generated considering the unsteady interaction between a cylinder's wall-bounded wake flow and a panel undergoing a forced motion. The database, used for the evaluation of Lagrangian Particle Tracking and Data Assimilation algorithms within the framework of the European project HOMER, considers two panel materials (metal and rubber), different densities of markers on the panel's surface and of flow tracers, different experimental

setups (only LPT cameras or combinations of LPT and DIC cameras), and different acquisition modes (time-resolved, two-pulse and four-pulse image acquisitions). The analysis of the LPT results showed that the particles' reconstructions along the cameras' viewing direction (Z-direction) suffered from 2 to 3 times higher uncertainty than the reconstructions in the other directions (X and Y). As expected, higher accuracy was obtained with the time-resolved image acquisition, followed by the four-pulse image acquisition. The uncertainty of the particles' reconstructions with the two-pulse strategy was twice as large as that of the time-resolved strategy. While the particles positions and velocities were reconstructed with high accuracy (uncertainties typically below 0.1 $\overline{px}$ and 1% of V_∞, respectively), larger errors were encountered for the particles' accelerations, typically ranging between 10% and 30% of the reference acceleration V_∞^2/D. Hence, it can be concluded that the accurate determination of the particles' Lagrangian accelerations is still a challenge that requires further improvements in the LPT algorithms. Finally, differences in performances were noticed between the DLR and the LaVision LPT algorithms, with the former typically yielding higher percentages of reconstructed particles and lower reconstruction errors.

From the analysis of the Data Assimilation results, it emerged that both the velocity and the pressure field suffered from errors of up to 10% of the reference values V_∞ and q_∞, respectively. These errors decrease to 5% for the velocity and 7% for the pressure when increasing the seeding concentration to the highest *ppp* of 0.16. Also, the use of the temporal information in the data assimilation algorithm yielded a slight increase in the measurement accuracy, especially for the velocity. When looking at the spatial power spectra of the velocity fluctuations, it was noticed that the higher *ppp* enabled to resolve accurately smaller turbulent structures in the flow. Flow scales of at least four times the inter-particle distance were correctly reconstructed with the DA algorithms.

The panel's position could be reconstructed within 5 μm accuracy (0.1% of the peak displacement) with both algorithms at the three *ppp* values. The reconstructed surface pressure followed closely the trend of the ground truth value, but exhibited both bias and random errors of the order of 10% q_∞.

References

Cakir, B. O., Sciacchitano, A., Saiz, G. G., & van Oudheusden, B. (2021, August). Dense flow field interpolations from PTV data in the presence of generic solid boundaries. In *14th International Symposium on Particle Image Velocimetry* (Vol. 1, No. 1).

Elsinga, G. E., Scarano, F., Wieneke, B., & van Oudheusden, B. W. (2006). Tomographic particle image velocimetry. *Experiments in fluids*, *41*(6), 933-947.

Gesemann, S., Huhn, F., Schanz, D., & Schröder, A. (2016, July). From noisy particle tracks to velocity, acceleration and pressure fields using B-splines and penalties. In 18th international symposium on applications of laser and imaging techniques to fluid mechanics, Lisbon, Portugal (Vol. 4, No. 7).

Jahn, T., Schanz, D., & Schröder, A. (2021). Advanced iterative particle reconstruction for Lagrangian particle tracking. *Experiments in Fluids*, *62*(8), 1-24.

Jeon, Y. J., Schneiders, J. F. G., Müller, M., Michaelis, D., & Wieneke, B. (2018, October). 4D flow field reconstruction from particle tracks by VIC+ with additional constraints and multigrid approximation. In Proceedings 18th International Symposium on Flow Visualization. ETH Zurich.

Jeon, Y. J. (2021, August). Eulerian time-marching in Vortex-In-Cell (VIC) method: reconstruction of multiple time-steps from a single vorticity volume and time-resolved boundary condition. In 14th International Symposium on Particle Image Velocimetry (Vol. 1, No. 1).

Kähler, C. J., Astarita, T., Vlachos, P. P., Sakakibara, J., Hain, R., Discetti, S., ... & Cierpka, C. (2016). Main results of the 4th International PIV Challenge. *Experiments in Fluids*, 57(6), 1-71.

Khojasteh, A. R., Yang, Y., Heitz, D., & Laizet, S. (2021). Lagrangian Coherent Track Initialisation (LCTI). arXiv preprint arXiv:2106.11049.

Lasinger, K., Vogel, C., Pock, T., & Schindler, K. (2018). Variational 3D-PIV with sparse descriptors. *Measurement Science and Technology*, 29(6), 064010.

Lasinger, K., Vogel, C., Pock, T., & Schindler, K. (2020). 3D fluid flow estimation with integrated particle reconstruction. *International Journal of Computer Vision*, 128(4), 1012-1027.

Mertens, C., Sciacchitano, A., van Oudheusden, B. W., & Sodja, J. (2021). An integrated measurement approach for the determination of the aerodynamic loads and structural motion for unsteady airfoils. *Journal of Fluids and Structures*, 103, 103293.

Mertens, C., de Rojas Cordero, T., Sodja, J., Sciacchitano, A., & van Oudheusden, B. W. (2022). Aeroelastic Characterization of a Flexible Wing Using Particle Tracking Velocimetry Measurements. *AIAA Journal*, *60*(1), 276-286.

Novara, M., Schanz, D., Reuther, N., Kähler, C. J., & Schröder, A. (2016). Lagrangian 3D particle tracking in high-speed flows: Shake-The-Box for multi-pulse systems. *Experiments in fluids*, *57*(8), 1-20.

Novara, M., Schanz, D., Geisler, R., Gesemann, S., Voss, C., & Schröder, A. (2019). Multi-exposed recordings for 3d lagrangian particle tracking with multi-pulse shake-the-box. *Experiments in Fluids*, *60*(3), 1-19.

Scarano, F., Schneiders, J. F., Saiz, G. G., & Sciacchitano, A. (2022). Dense velocity reconstruction with VIC-based time-segment assimilation. *Experiments in Fluids*, *63*(6), 1-15.

Schanz, D., Gesemann, S., & Schröder, A. (2016). Shake-The-Box: Lagrangian particle tracking at high particle image densities. *Experiments in fluids*, *57*(5), 1-27.

Schneiders, J. F., & Scarano, F. (2016). Dense velocity reconstruction from tomographic PTV with material derivatives. *Experiments in fluids*, *57*(9), 1-22.

Sciacchitano, A., Leclaire, B., & Schroeder, A. (2021a). Main results of the first lagrangian particle tracking challenge. In *Proceedings of 14th International Symposium on Particle Image Velocimetry* (Vol. 1, No. 1, pp. 1-14). ILLINOIS Tech/Paul V. Galvin Library.

Sciacchitano, A., Leclaire, B., & Schroeder, A. (2021b). Main results of the first Data Assimilation Challenge. In *Proceedings of 14th International Symposium on Particle Image Velocimetry* (Vol. 1, No. 1, pp. 1-13). ILLINOIS Tech/Paul V. Galvin Library.

Van Gent, P. L., Michaelis, D., Van Oudheusden, B. W., Weiss, P. É., de Kat, R., Laskari, A., ... & Schrijer, F. F. J. (2017). Comparative assessment of pressure field reconstructions from particle image velocimetry measurements and Lagrangian particle tracking. *Experiments in Fluids*, *58*(4), 1-23.

Wieneke, B. (2012). Iterative reconstruction of volumetric particle distribution. *Measurement Science and Technology*, *24*(2), 024008.

Yang, Y., & Heitz, D. (2021). Kernelized Lagrangian particle tracking. *Experiments in Fluids*, *62*(12), 1-27.

Yang, Y., Heitz, D., & Mémin, E. (2019, July). Lagrangian particle image velocimetry. In *ISPIV2019-13th International Symposium on Particle Image Velocimetry* (pp. 1-9).